Supplementary Information

Size Dependent CO_2 Reduction Activity of Ag Nanoparticle Electrocatalysts

Xingyi Deng,[*,1,2] Dominic Alfonso,[*,1] Thuy-Duong Nguyen-Phan,[1,2] and Douglas R. Kauffman[*,1]

1. National Energy Technology Laboratory, 626 Cochrans Mill Road, P.O. Box 10940, Pittsburgh, PA 15236-0940, USA

2. NETL Support Contractor, 626 Cochrans Mill Road, P.O. Box 10940, Pittsburgh, PA 15236-0940, USA

***Email:** Xingyi.Deng@NETL.DOE.GOV; Dominic.Alfonso@NETL.DOE.GOV;

Douglas.Kauffman@NETL.DOE.GOV

Computational Methods

Density Functional Theory Calculations

Structure relaxations and single point energies were calculated using the density functional theory (DFT) as implemented in the Vienna *Ab Initio* Simulation Package (VASP) commercial software.[1] The projector-augmented wave (PAW) pseudopotential was utilized to treat the core electrons while the Perdew, Burke and Enzerhoff (PBE) exchange-correlation functional of the generalized gradient approximation (GGA) was used for describing the electron interactions.[2, 3] A plane wave cutoff energy of 520 eV for the Kohn-Sham one electron valence eigenstates was adopted for all calculations. Periodic Ag(111) and Ag(100) slab models were used to represent the active sites on the low-index plane of the metal catalyst. Edge sites were represented using the internal step edge of a Ag(211) surface, as has been done previously.[4] We used (3 × 3), (4 × 4) and (2 × 4) surface unit cells for the (111), (100) and Ag edge site (Ag(211) step edge) surfaces with thickness of four, four and ten layers, respectively. The vacuum space in the *z*-direction was set to 12 Å to prevent the interaction between periodic images. The lattice constant of the various slabs was fixed to the value obtained from optimizing with DFT this constant for the bulk metal. The computed lattice constants for the bulk Ag is 4.17 Å which compares well with the experimental value of 4.09 Å found in the literature.[5] To represent the corner sites, an icosahedral 147 atom Ag cluster (Ag_{147}) enclosed in a periodic 30 Å × 30 Å × 30 Å box was utilized.[4]

The reciprocal space for Ag(111), Ag(100) and edge site (Ag(211) step edge) models was sampled with a Monkhorst-Pack *k*-point mesh of $3 \times 3 \times 1^6$ while for Ag_{147}, the Γ-point sampling is used Geometry optimization was carried out until the maximal residual force was < 0.03 eV/ Å. A Methfessel-Paxton smearing of $\sigma = 0.2$ eV was utilized to improve convergence and the corrected energy for $\sigma \rightarrow 0$ was employed. Solvent corrections were taken into account using the

Poisson-Boltzmann implicit solvent model implemented in VASP by Matthew and Hennig.[7] The background dielectric constant of water is $\varepsilon_b = 80$ with a cutoff charge density of 0.0025 $Å^{-3}$. The cavitation energies were evaluated employing a surface tension parameter of 0.525 meV/ $Å^2$.

Microkinetic Modeling

The approach for the microkinetic simulations was as follows. The forward rate constant for an electrochemical surface reaction step of the type, $*A + H^+ + e^- \rightarrow *AH$ was calculated using transition state theory.[8, 9, 10]

$$k_f = \frac{k_B T}{h} exp\left(-\frac{\Delta G^{\#}(U)}{k_B T}\right) \quad (3)$$

where k is the rate coefficient in s^{-1}, k_B is the Boltzmann constant, T is the temperature in K, and h is the Planck's constant. $\Delta G^{\#}(U)$ is the potential-dependent reaction barrier given by

$$\Delta G^{\#}(U) = \Delta G^{\#}(U^o) + \beta e(U - U^o) \quad (4)$$

where $\Delta G^{\#}(U^o)$ is the barrier at the reversible potential U^o, and β is a symmetry factor which is typically set to 0.5. The term U^o is given by

$$U^o = -\frac{\Delta G(U=0\ vs\ SHE)}{e} \quad (5)$$

where $\Delta G(U = 0\ vs\ SHE)$ is the reaction free energy at 0V vs SHE (standard hydrogen electrode). This term is calculated using the computational hydrogen electrode model (CHE).[11] This framework takes advantage of the equivalence of the free energies of the proton-electron pair ($G_{H^+ + e^-}$) and hydrogen gas ($\frac{1}{2}\ G_{H_{2(g)}}$) at 0 V to rigorously evaluate the chemical potential of the electrode/electrolyte species. The relationship allows equating their free energies and applying a

linear shift in potential by $-eU$ where U is on the SHE scale. The reaction free energy of *A + $H^+_{(aq)}$ + e^- → *AH* at a given applied potential U is then given by $\Delta G(U) = G_{*AH} - G_{*A} - \frac{1}{2}G_{H_{2(g)}} + eU$, where G_{*AH}, G_{*A}, $G_{H_{2(g)}}$ and e are the free energy of the product, free energy of the reactant, free energy of gas phase H_2 and the elementary positive charge To ensure thermodynamic consistency, the reverse rate constant is calculated from the thermodynamic equilibrium constant, K_{eq}.

$$K_{eq} = exp\left(-\frac{e(U-U^o)}{k_B T}\right) \;\; ; \;\; k_r = \frac{k_f}{K_{eq}} \qquad (6)$$

With rate constant defined, a system of coupled ordinary differential equations is developed to represent a microkinetic model. The derivative of concentration of surface intermediates over time for each species is obtained as follows:

$$\frac{d\theta_i}{dt} = \sum_j v_{i,j}\, r_j \qquad (7)$$

where j loops over all elementary reaction step, θ_i is the dimensionless fractional coverage of surface intermediate species i while $\upsilon_{i,j}$ is the stoichiometric coefficient of species i in the elementary reaction step j. The simulations were initialized with clean surfaces and the given set of ordinary differential equations, $\{d\theta_i/dt\}$, were integrated with respect to time using a Python-based ODE solver to determine the steady-state coverages and turnover frequencies. We considered the following mechanism:[12, 13]

(i) $CO_2 + H^+_{(aq)} + e^- + * \rightarrow *COOH$

(ii) $*COOH + H^+_{(aq)} + e^- \rightarrow *CO + H_2O$

(iii) $*CO \rightarrow CO + *$

(iv) $H^+_{(aq)} + e^- + * \rightarrow *H$

(v) $*H + *H \rightarrow H_2 + 2*$

where * denotes either a free site or a bound intermediate. The climbing image nudged elastic band (CI-NEB) method was used to predict the transition state geometries and energies.[14] For step (IV), the barrier is determined using H_3O^+ as the proton source.[15] To determine the barrier for (I) and (II), we used an equivalent hydrogenation reaction of the type, $A + *H \rightarrow *AH$.[16] In this case, U^o is equal to the negative of the free energy of adsorption of *H for a particular surface, $-\Delta G_{*H,ads}$. We used the H-shuttling model where a hydrogen is transferred to the target adsorbate through the assistance of 1-2 H_2O.[16] All transition states were referenced to the initial state of aqueous protons and electrons which is quantified using the CHE method.[11] For analysis of a number of transition states, Bader charge analysis was carried out.[17] The net electronic charge was used to quantify the point charge of a given ion, which is defined as difference between the number of electrons on the ion and a free-standing neutral atom.

Experimental Faradaic efficiencies calculations and corrections

Details of calculating Faradaic efficiencies of the Ag/HOPG catalysts for each product, including corrections made by subtracting the HOPG contributions, are described below:

The Faradaic efficiency for product i was calculated using the following equation (A):

$$FE(i) = \frac{Z(i) \times F \times n(i)}{Q} \times 100\%$$

where Z(i) is the number of electrons involved in the formation of i product (Z = 2 for both CO and H_2), F is the Faraday's constant (96485 C/mol); n(i) is the moles of product i formed (determined by GC); and Q is the total charge measured by the potentiostat.

All catalysts in this work contained Ag loadings < 7 nmol/cm^2, which is several orders of magnitude lower than typical loadings of conventional catalysts. Background electrochemical contributions from catalyst-free regions of the HOPG substrate cannot be neglected in this low-loading regime, and we subtracted HOPG contributions from the raw data to calculate the intrinsic Faradaic efficiencies of Ag catalysts using the following equation (B):

$$FE(i) = \frac{Z(i) \times F \times [n(i) - \chi \times m(i)]}{[Q(n) - \chi \times Q(m)]} \times 100\%$$

Here, Z(i) is the number of electrons involved in the formation of i product (Z = 2 for both CO and H_2), F is the Faraday's constant (96485 C/mol); n(i) and m(i) are the moles of product i formed on Ag/HOPG catalysts and on HOPG, respectively (determined by GC). Q(n) and Q(m) are the measured electrolysis charge for the Ag/HOPG catalysts and a catalyst-free HOPG substrate, respectively. χ is the fraction of exposed HOPG area in the Ag/HOPG catalysts compared with the freshly cleaved HOPG, as estimated by XPS based on the C 1s peak attenuation (comparing the C 1s peak intensity of the Ag/HOPG samples with the freshly cleaved HOPG). Selected electrochemical data for calculating raw Faradaic efficiencies and intrinsic Faradaic efficiencies of the HOPG supported Ag catalysts are shown in Table S2.

Table S1. Reaction barriers associated with the rate determining step ($\Delta G^{\#}_{max}$) and forward rate constants (k_f) for CO_2RR and HER at -1V *vs.* the standard hydrogen electrode (SHE). Here, $\Delta G^{\#}_{max}$ represent the largest reaction free energy barrier within the CO_2RR or HER mechanism at -1V *vs.* SHE, and k_f was calculated as $k_f = \frac{k_B T}{h} exp\left(-\frac{(\Delta G^{\#}_{max})}{k_B T}\right)$ as described in the methods section.

Site	CO_2RR $\Delta G^{\#}_{max}$ (eV)	HER $\Delta G^{\#}_{max}$ (eV)	CO_2RR k_f (s^{-1})	HER k_f (s^{-1})
Ag(100)	0.426	0.974	$3.88x10^{5}$	$2.12x10^{-4}$
Edge	0.477	0.875	$5.37x10^{4}$	$9.74x10^{-3}$
Ag(111)	0.904	1.094	$3.23x10^{-3}$	$1.96x10^{-6}$
Corner	1.319	1.099	$3.08x10^{-10}$	$1.64x10^{-6}$

Table S2. Selected electrochemical data for calculating raw Faradaic efficiencies and intrinsic Faradaic efficiencies of the Ag/HOPG catalysts at E = -1.2 V vs. RHE.

Ag loading ($nmol/cm^2$)	Average particle diameter (nm)	Electrolysis charge (C)	Produced CO (nmol)	Produced H_2 (nmol)	Raw FE_{CO} (%)[(a)]	Raw FE_{H2} (%)[(a)]	Exposed HOPG Surface (%)[(b)]	HOPG-subtracted FE_{CO} (%)[(c)]	HOPG-subtracted FE_{H2} (%)[(c)]	Total HOPG-Subtracted FE (%)
0 (HOPG)	n/a	0.1670	37.3	BDL[(d)]	4.43	n/a	1	n/a	n/a	n/a
1.0	5.3	0.2819	234	352	16.08	24.10	0.928	30.33	53.54	83.9
1.2	6.0	0.2664	317	278	23.00	20.12	0.861	44.87	43.78	88.7
1.3	6.4	0.2522	394	196	30.20	14.97	0.861	64.43	34.89	99.3
2.0	7.7	0.2804	709	45.6	48.80	3.14	0.799	89.18	5.99	95.2
2.4	8.7	0.3752	1250	13.8	64.4	0.71	0.792	96.97	1.10	98.1
3.3	9.0	0.3865	1380	26.3	68.7	1.31	0.653	94.30	1.83	96.1
4.4	9.9	0.5323	2290	8.44	82.9	0.31	0.551	99.47	0.37	99.8
27.4[(e)]	Bulk foil	2.2791	10600	457	89.87	3.87	n/a	n/a	n/a	93.7

(a) Calculated based on equation (A).
(b) The fraction of exposed HOPG area in the Ag/HOPG catalysts compared with the freshly cleaved HOPG, estimated by XPS based on the C 1s peak attenuation (comparing the C 1s peak intensity of the Ag/HOPG samples with the freshly cleaved HOPG).
(c) Calculated based on equation (B).
(d) BDL: Below detection limit for the gas chromatograph.
(e) Estimated by comparing the Ag 3d XP peak intensity of the Ag foil to those of the Ag/HOPG samples.

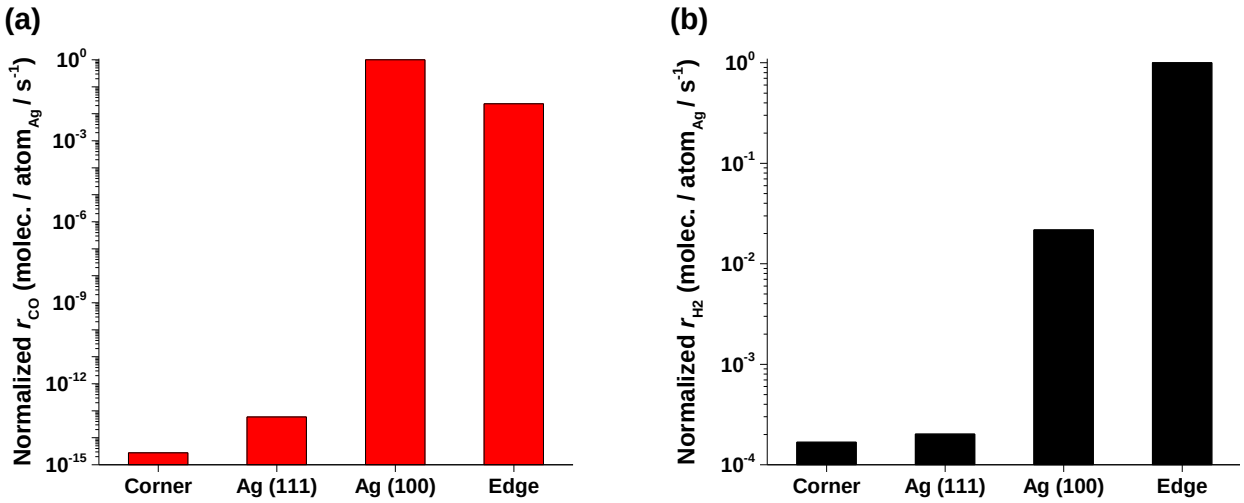

Figure S1. Normalized MKM-predicted rates for (a) CO and (b) H_2 production at -1V *vs.* SHE at various Ag sites. The rates were normalized to highest activity among the sites for each reaction.

Here we compared the normalized rates for CO_2RR and HER at each catalyst site. The rates were normalized to the site with highest value for each reaction. As Norskøv and coworkers previously mentioned,[18] quantitative comparison between MKM-determined rates is not always appropriate due to intrinsic errors and uncertainties in DFT-based calculations. Therefore, we compared the relative activity of each reaction to identify relative trends in CO_2RR and HER activity.

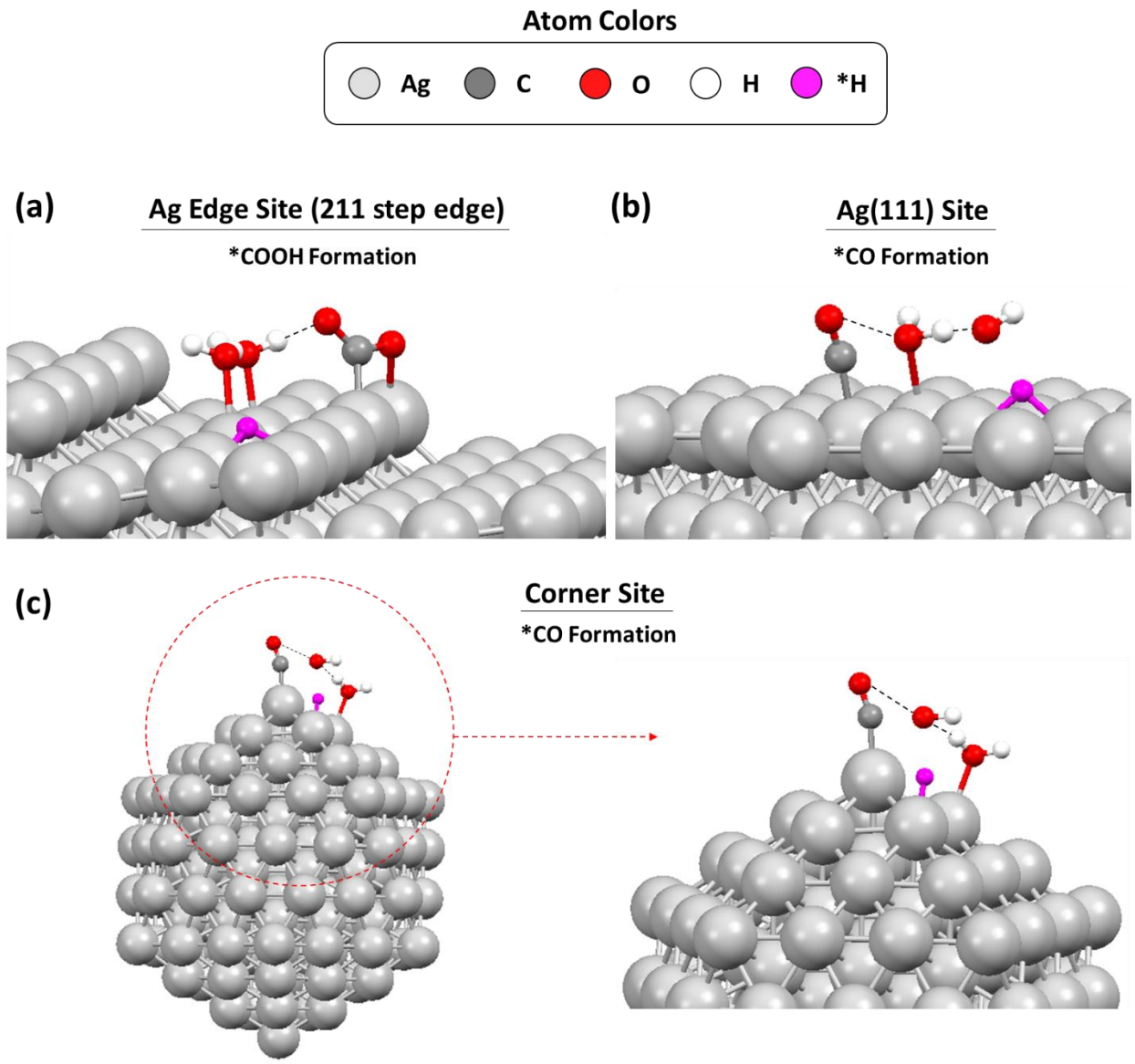

Figure S2. CO_2RR transition state geometries at -1V *vs.* SHE; atom colors are provided in the legend. (a) *COOH formation at Ag edge sites, as modeled using the step edge of a Ag(211) surface.[4] (b) *CO formation at a Ag(111) site. (c) *CO formation at an Ag corner site. The *H species originated from water and represent the transfer of H^+/e^- pairs. The *CO formation transition state at Ag(111) and Ag corner sites involved the stabilization of OH^- by an absorbed $*H_2O$ molecule after it was cleaved from *COOH. *Note:* the *H binding location at corner sites is identical to those found for the HER transition state shown in Figure S3.

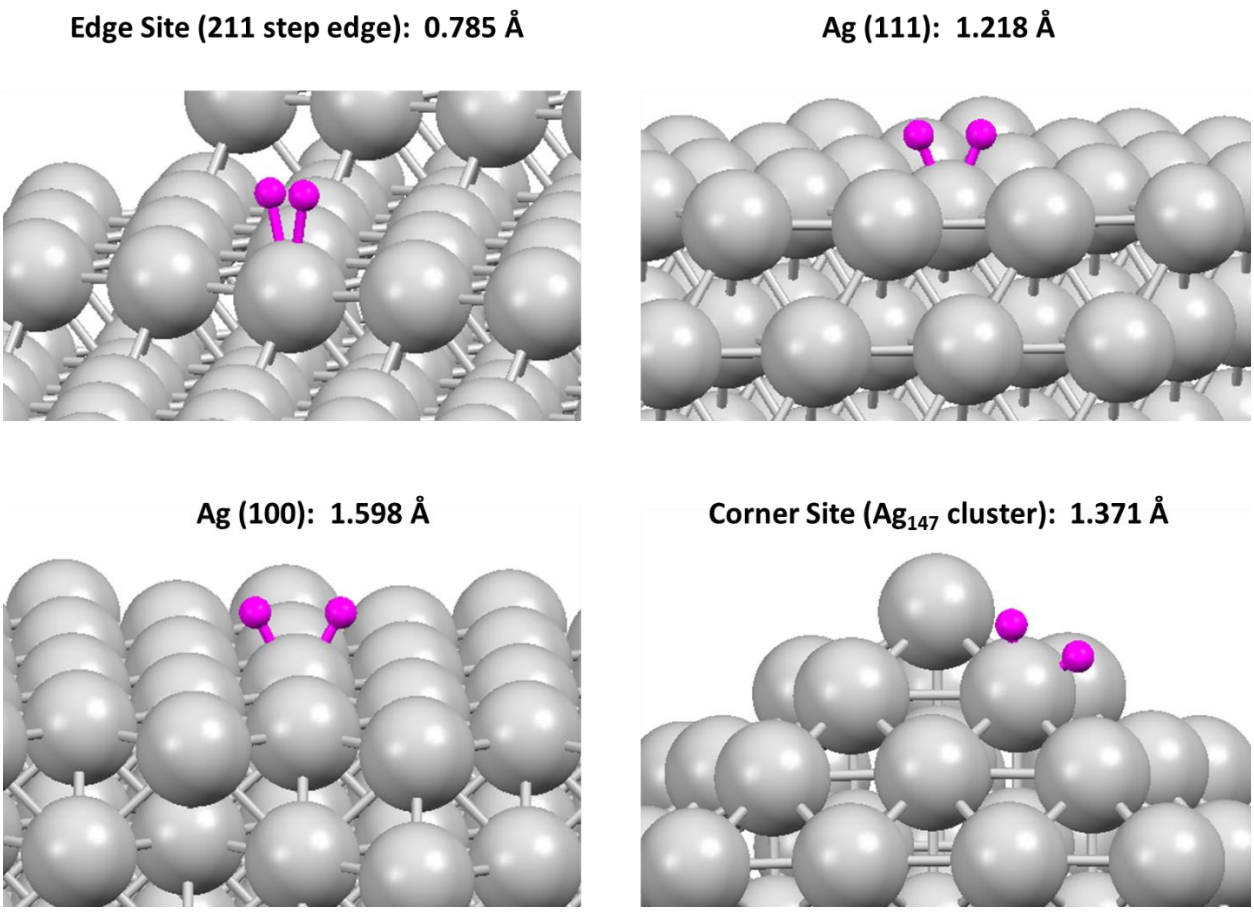

Figure S3. HER transition states of each site with *H distances indicated. Interestingly, *H preferred to form adjacent to the corner atom of the Ag_{147} cluster model, and an identical *H location was also found for the CO_2RR transition state shown in Figure S2c.

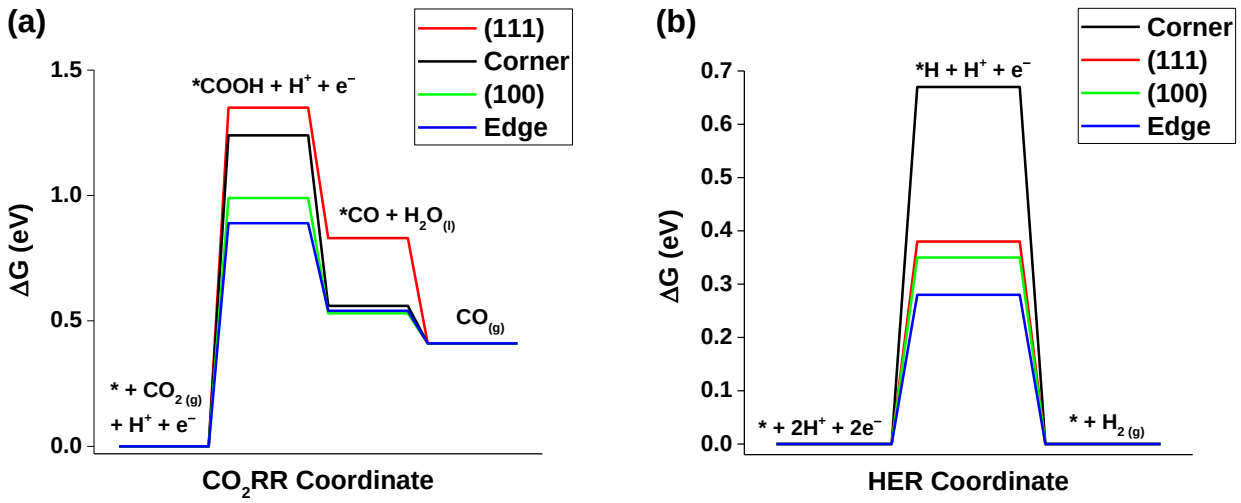

Figure S4. Gibbs free energy changes for (a) CO_2RR and (b) HER at 0 V *vs.* SHE. *Note*: these Gibbs free energy changes do not include transition state barriers and represent thermodynamic barriers at an electrochemical potential of 0 V *vs.* SHE.

The results in Figure S4 largely agree with previous thermodynamic calculations that identified *COOH and *H formation as the most thermodynamically challenging (*i.e.* potential limiting) CO_2RR and HER step for various Ag active sites.[4] However, the inclusion of transition state barriers is required to determine the kinetically rate limiting step, as discussed in the main text.

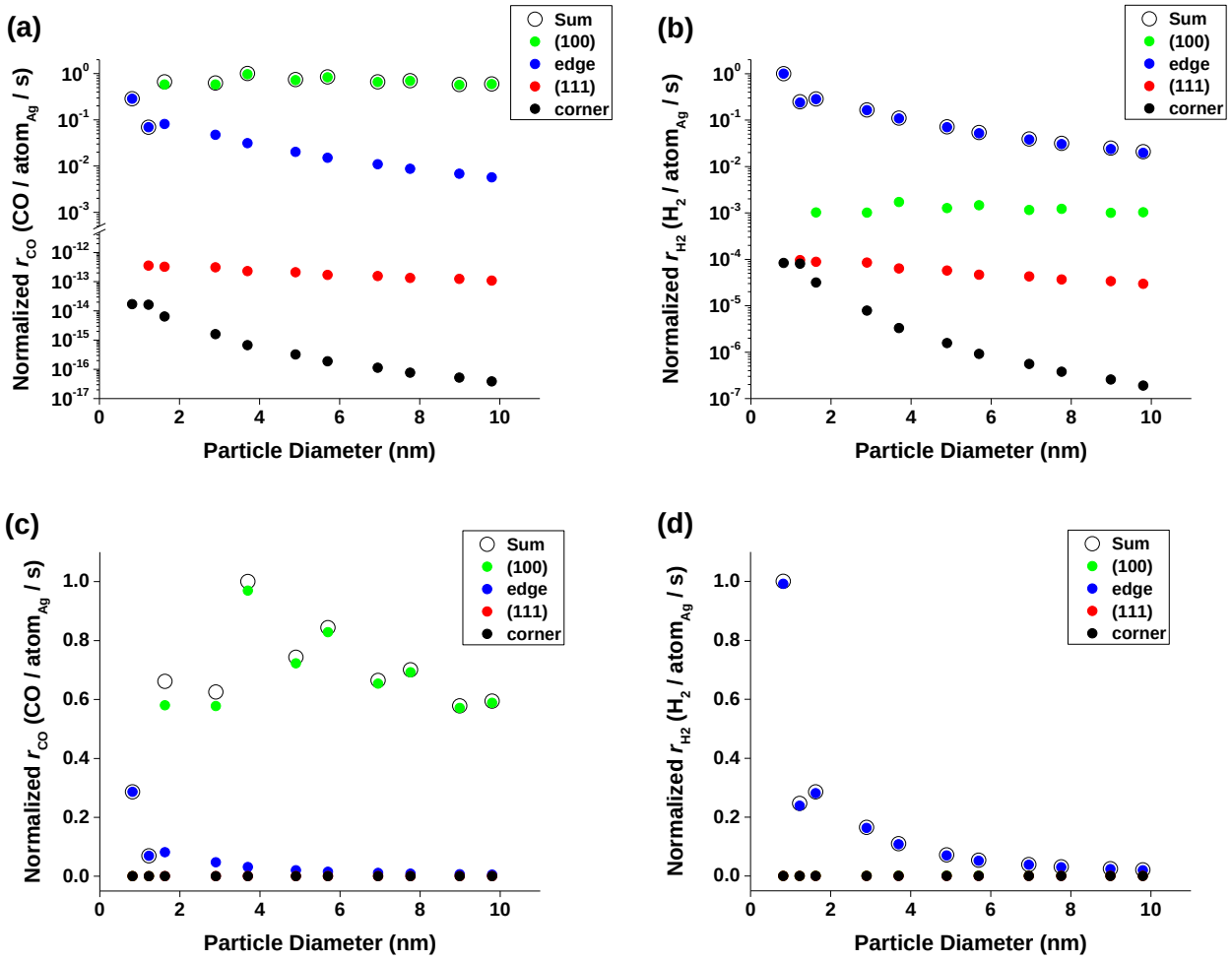

Figure S5. (a,b) Log_{10} scale and (c,d) linear scale presentation of deconvoluted, site-specific r_{CO} and r_{H2} for various NP sizes at -1.0 V *vs.* SHE. The total rate is indicated with the "sum" labels.

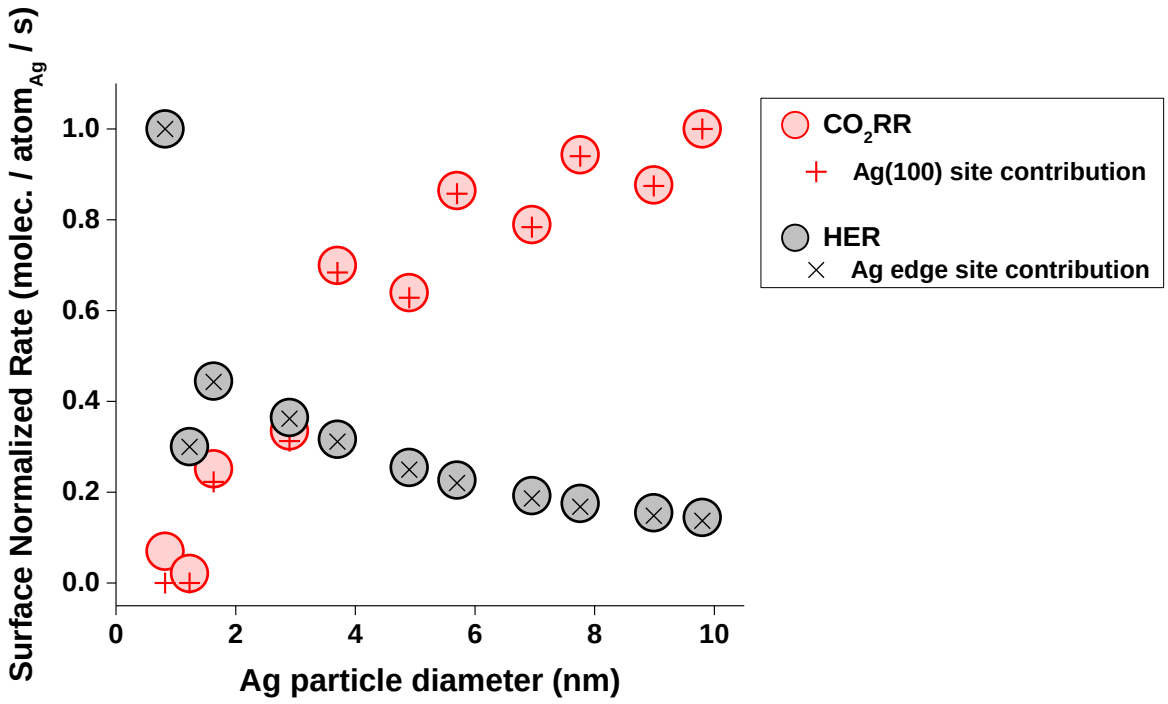

Figure S6. Surface normalized CO_2RR and HER rates from MKM calculations. These rates only consider electrochemically-accessible surface atoms and exclude electrochemically-inaccessible bulk (interior) atoms. Ag(100) and Ag edge sites were the dominant contributors to CO_2RR and HER rates, respectively, similar to what is presented in main text Figure 2c.

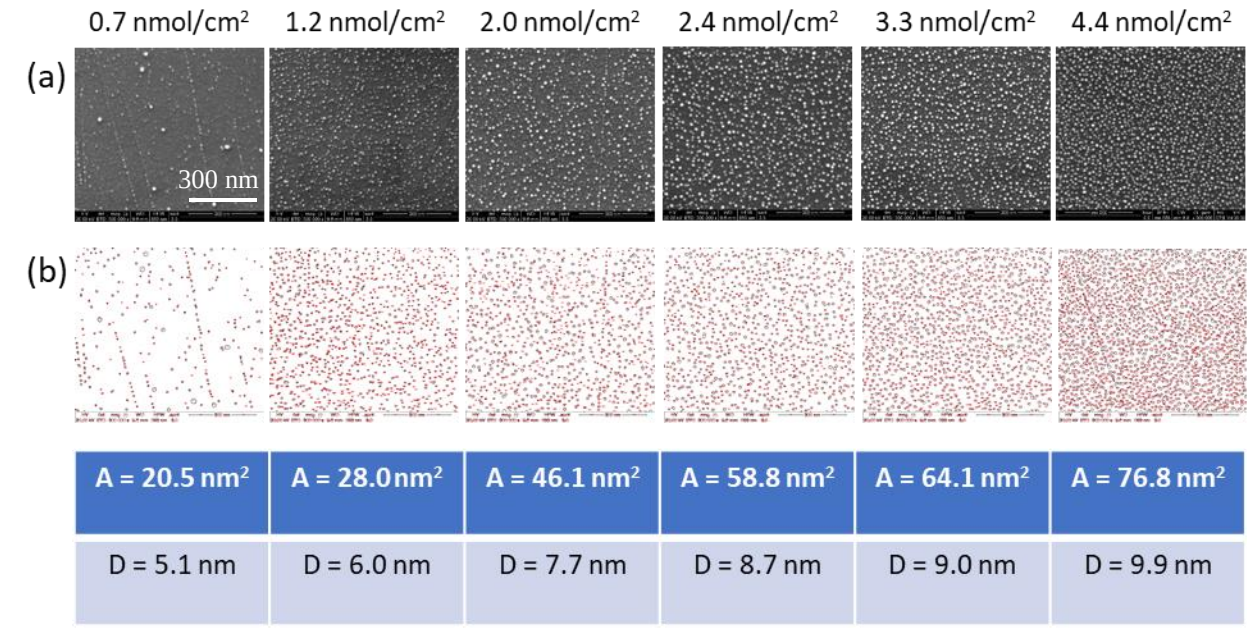

(c)

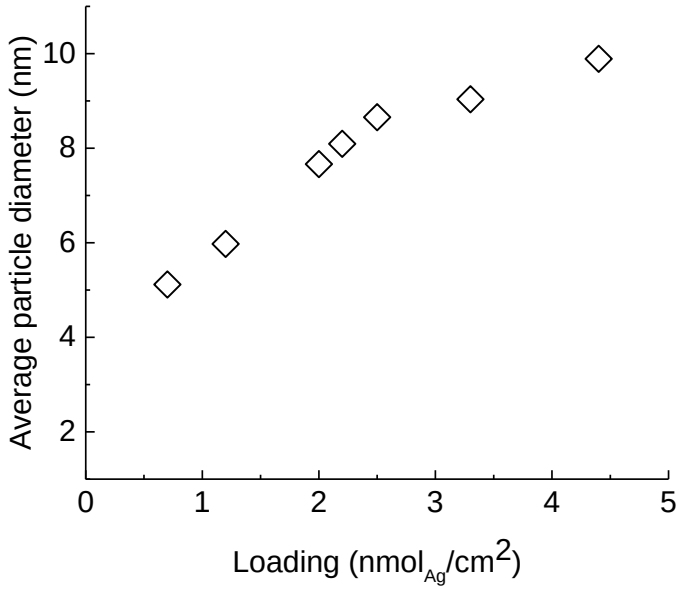

Figure S7. (a) Scanning electron microscopy (SEM) images of Ag/HOPG catalysts with increasing Ag loading prepared via e-beam assisted evaporation in an ultrahigh vacuum (UHV) chamber, and (b) corresponding "analyzed" SEM images using ImageJ software (version 1.52a) to quantify the average particle area (A/nm^2) and average particle diameter (D/nm). (c) Average Ag particle diameter versus Ag loading for the UHV-prepared Ag/HOPG catalysts.

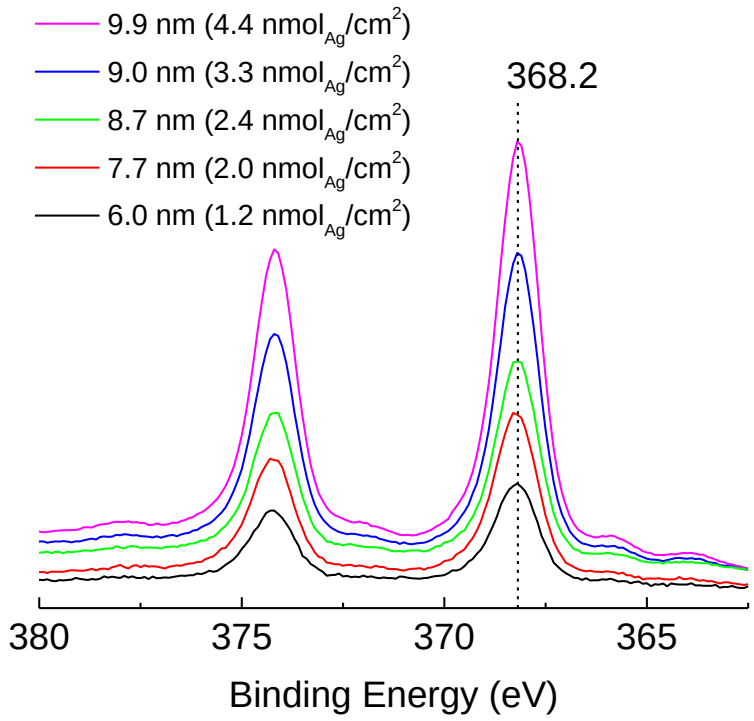

Figure S8. Ag 3d X-ray photoelectron spectra of Ag/HOPG catalysts with different loading, showing Ag all in the metallic state.

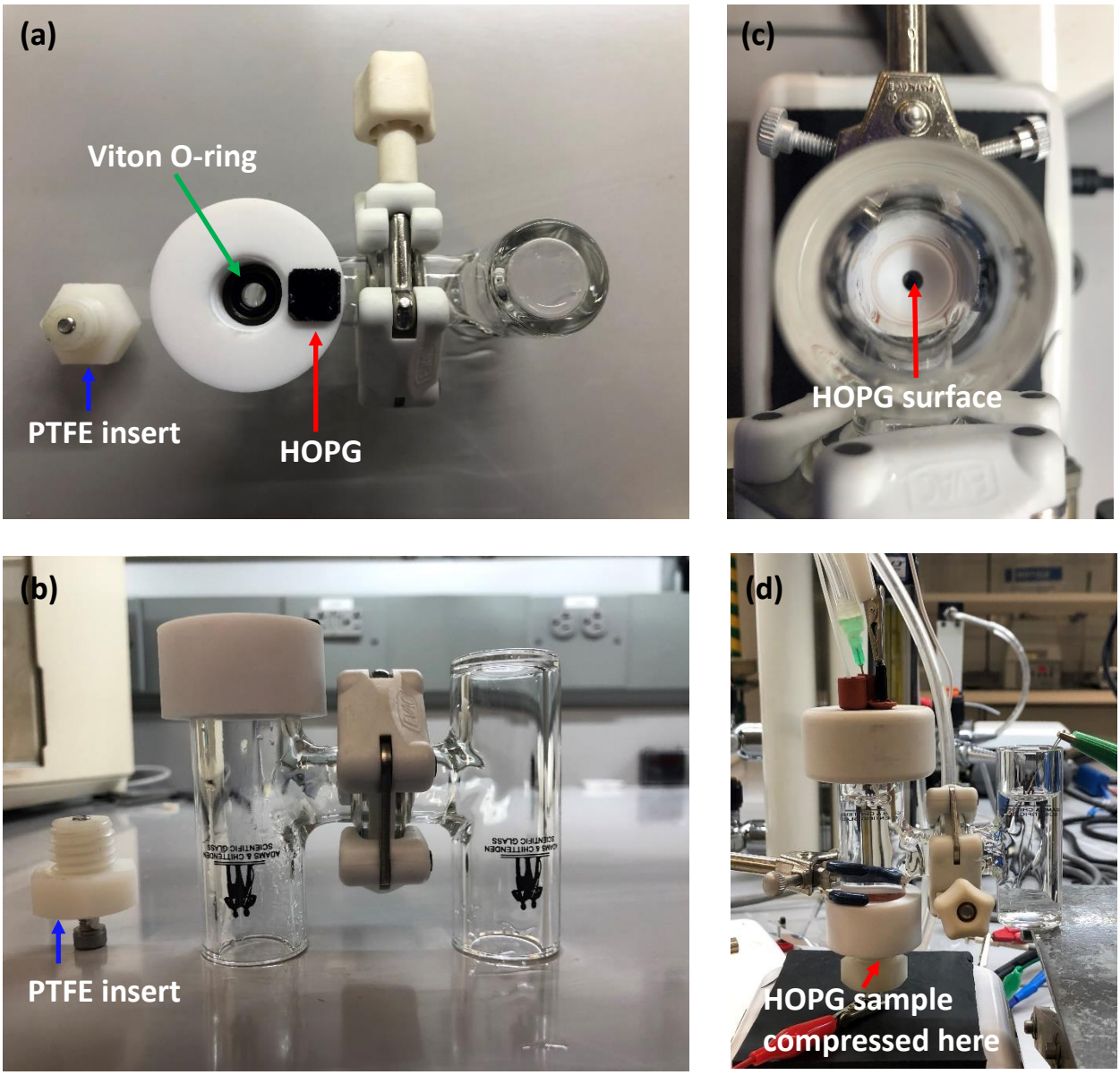

Figure S9. Pictures of the gas-tight H-cell and custom electrode holder used for the HOPG-supported samples. (a) Bottom view. (b) Side view. (c) Top view of the catholyte chamber with a HOPG sample compressed against the 7 mm inner diameter Viton O-ring using the threaded PTFE insert. (d) Fully assembled H-cell for CO_2RR and HER measurements.

The flat HOPG substrate was loaded into a custom H-Cell lid that sealed the bottom of the catholyte chamber. A threaded PTFE insert with an electrical feed-through compressed the HOPG surface against a Viton O-ring, ensured a consistent 0.38 cm^2 geometric electrode area, and made electrical contact with the backside of the HOPG.

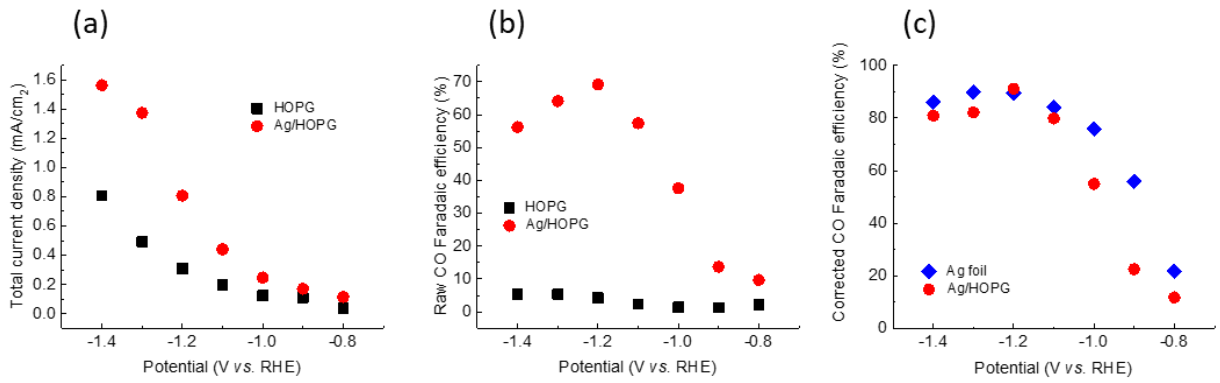

Figure S10. Potential dependent (a) total current density and (b) raw FE_{CO} of 9 nm, HOPG-supported Ag nanoparticles (3.3 $nmol_{Ag}/cm^2$) and a clean (catalyst free) HOPG substrate in CO_2-saturated 0.1M $KHCO_3$. (c) Comparison between the potential dependent FE_{CO} of a polycrystalline Ag foil and 9 nm Ag nanoparticles (3.3 $nmol_{Ag}/cm^2$) after subtracting contributions from the HOPG substrate. A maximum FE_{CO} > 90% was observed for the Ag nanoparticles at E = -1.2 V *vs.* RHE.

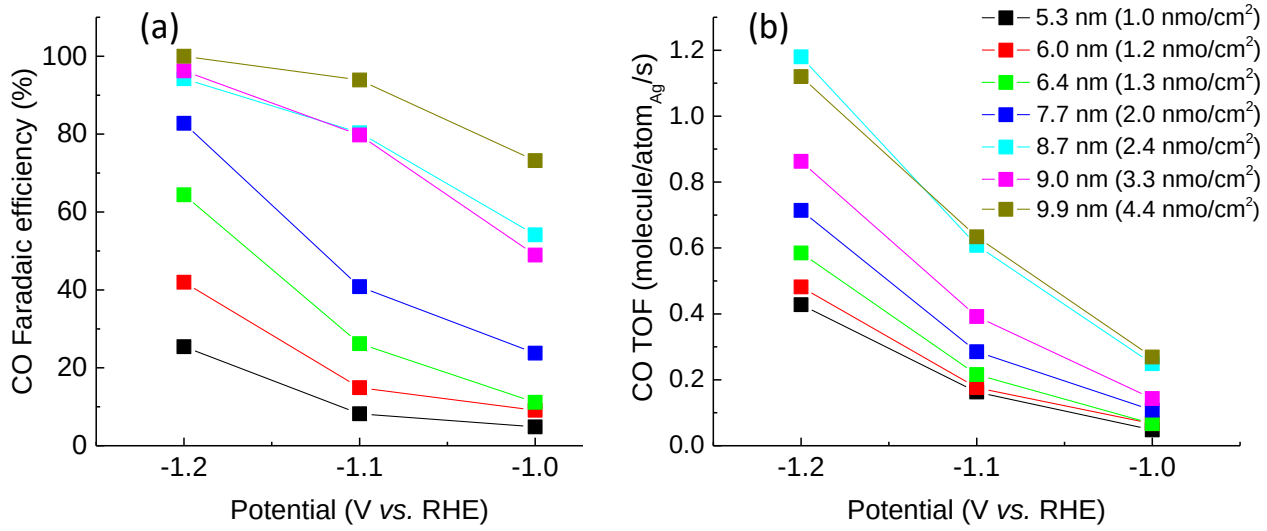

Figure S11. Size-dependent (a) FE_{CO} and (b) TOF_{CO} of the Ag nanoparticles in CO_2 saturated 0.1 M $KHCO_3$ electrolyte at various potentials. Contributions from the HOPG substrate were subtracted. The lower FE_{CO} at smaller potentials is consistent with the potential dependent CO of Ag NPs and bulk Ag, but low current density produced in this low loading regime made H_2 quantification difficult below -1.2V *vs.* RHE due to the GC's TCD detection limit.

References.

1. Kresse G, Furthmüller J. Effeciency of Ab-Initio Total Energy Calculations for Metals and Semiconductors Using a Plane-Wave Basis Set *Comp Mat Sci* **6**, 15-50 (1996).

2. Kresse G, Joubert D. From Ultrasoft Pseudopotentials to the Projector Augmented Wave Method. *Phys Rev B* **59**, 1758-1775 (1999).

3. Perdew JP, Burke K, Enzerhof M. Generalized Gradient Approximation Made Simple. *Phys Rev Lett* **77**, 3865-3868 (1996).

4. Back S, Yeom MS, Jung Y. Active Sites of Au and Ag Nanoparticle Catalysts for CO_2 Electroreduction to CO. *ACS Catal* **5**, 5089-5096 (2015).

5. Kittel C. *Introduction to Solid State Physics*, 6th edn. Wiley (1986).

6. Monkhorst HJ, Pack JD. Special Points for Brillouin-Zone Integrations. *Phys Rev B* **13**, 5188-5192 (1976).

7. Matthew K, Sundararaman R, Lechtworth-Weaver K, Arias TA, Hennig R. *J Chem Phys* **140**, 084106 (2014).

8. Eyring H. The Activated Complex in Chemical Reactions. *J Chem Phys* **3**, 107-115 (1935).

9. Evans MG, Polanyi M. Inertia and Driving Force of Chemical Reactions. *Trans Faraday Soc* **34**, 11-24 (1938).

10. Chen LD, Urushihara M, Chan K, Nørskov JK. Electric field effects in electrochemical CO2 reduction. *ACS Catal* **6**, 7133-7139 (2016).

11. Norskov JK*, et al. J Phys Chem B* **108**, 17886-17892 (2004).

12. Peterson AA, Abild-Pedersen F, Studt F, Rossmeisl J, Nørskov JK. How copper catalyzes the electroreduction of carbon dioxide into hydrocarbon fuels. *Energy Environ Science* **3**, 1311-1315 (2010).

13. Hansen HA, Varley JB, Peterson AA, Nørskov JK. Understanding trends in the electrocatalytic activity of metals and enzymes for CO2 reduction to CO. *J Phys Chem Lett* **4**, 388-392 (2013).

14. Henkelman G, Uberuaga BP, Jónsson H. A Climbing Nudged Elastic Band Method for Finding Saddle Points and Minimum Energy Paths. *J Chem Phys* **113**, 9901-9904 (2000).

15. Liu X*, et al.* pH effects on the electrochemical reduction of CO (2) towards C 2 products on stepped copper. *Nature Communications* **10**, 1-10 (2019).

16. Nie X, Luo W, Janik MJ, Asthagiri A. Reaction mechanisms of CO2 electrochemical reduction on Cu (1 1 1) determined with density functional theory. *J Catal* **312**, 108-122 (2014).

17. Tang W, Sanville E, Henkelman G. A Grid-Based Bader Analysis Algorithm Without Lattice Bias. *J Phys Condens Matter* **21**, 084204 (2009).

18. Liu X, Xiao J, Peng H, Hong X, Chan K, Nørskov JK. Understanding Trends in Electrochemical Carbon Dioxide Reduction Rates. *Nat Commun* **8**, 15438 (2017).